

---

## The FOCI™ algorithm for seismic depth migration

Gary F. Margrave, Saleh M. Al-Saleh, Hugh D. Geiger, and Michael P. Lamoureux

### ABSTRACT

The FOCI algorithm is a new approach to the design and implementation of explicit wavefield extrapolation for depth migration in the space-frequency domain. Operator instability is addressed by splitting the operator into two parts, one that controls phase accuracy and another that improves stability. The first operator is simply a windowed version of the exact operator for a half-step. The second operator is designed as a band-limited inverse for the first. The final FOCI operator is formed as the convolution of the first operator with the conjugate of the second. By controlling the degree of evanescent filtering, the resulting operator can easily be stabilized for several thousand steps. During the wavefield extrapolation process, the data are divided into frequency chunks that are optimally resampled in the spatial coordinates to enhance the performance of the extrapolation. Lower frequencies are resampled to a larger sample size. Testing of the algorithm shows that it scales over three orders of magnitude as  $O(N)$  with run times comparable to the phase shift method of time migration. Images from trial depth migrations of the Marmousi model show very high resolution.

### INTRODUCTION

The many methods for seismic depth migration are often considered to fall into two broad classes: (1) Kirchhoff methods and (2) wave-equation methods. Kirchhoff methods are presently the dominant technique largely because of their lower computational effort and their adaptability to irregular recording geometries. The primary weakness of the Kirchhoff approach is its reliance on ray theory. The resulting seismic images generally contain only information that travels along Snell's law raypaths. Wave-equation methods, also called recursive extrapolation methods or wavefield marching methods, in principle allow energy to propagate along all possible paths and are widely acknowledged to produce a superior, image. However, these methods have not proven popular for two main reasons (1) they are computationally expensive and (2) the extrapolation operator is usually mathematically unstable. The FOCI method is a wavefield marching scheme that alleviates both of these concerns using three novel ideas: (1) stabilization by Wiener filter design, (2) reduced evanescent filtering, and (3) spatial down-sampling.

The theoretical wavefield extrapolator has infinite spatial extent. A simple way to gain computational efficiency is to localize this operator. Unfortunately, simple methods of localization such as spatial windowing usually lead to operator instability. A method to stabilize the operator was introduced by Hale (1991), and this remains the standard today. Hale recommended expanding the theoretical operator in a long Taylor series and then approximating the series with a special set of basis functions. While Hale's method does lead to stable operator designs, it is numerically and analytically cumbersome and can have less than desirable phase accuracy. As well, a simple change of the operator length using Hale's method usually requires the use of both symbolic and numerical

mathematical software packages. More recently, Thorbecke et al. (2004) have introduced a weighted least-squares method that is far easier to use than Hale's approach. Like FOCI, the techniques used by Thorbecke et al. result in extrapolators that are not perfectly stable but have a controlled instability. Thorbecke et al. are able to design operators that remain stable for 500 steps. With a typical step size of 10m, this allows imaging down to 5000 m, which is sufficient for many industrial applications.

We begin with a short theoretical background that extends the exact constant velocity phase-shift extrapolators in the wavenumber-frequency domain to approximate space-frequency domain extrapolators suitable for laterally varying velocities. We then discuss the FOCI method of designing a compactly supported approximation to the desired operator. Then follows a series of examples beginning with operator amplitude and phase spectra, moving on to impulse responses, to post stack depth migration and finally to pre stack depth migration. The full migrations are all done with the Marmousi model.

### THE FOCI™ METHOD

“FOCI” is an acronym for *forward operator and conjugate inverse* which suggests the key FOCI concept in operator stabilization by Wiener filtering. However, there are three key innovations in the method: (1) operator stabilization by Wiener filtering, (2) the use of dual operator tables to reduce evanescent filtering, and (3) spatial downsampling of the lower frequencies to increase operator accuracy and decrease run times.

#### Theoretical Background

Consider the equation for the f-k phase-shift extrapolator (Gazdag, 1978), written for wavefield marching in the z direction

$$\psi(x_T, z, \omega) = \frac{1}{(2\pi)^{n-1}} \int_{-\infty}^{\infty} \varphi(k_T, z=0, \omega) [e^{ik_z z}] e^{-ik_T \cdot x_T} dk_T \quad (1)$$

where the number of dimension  $n$  is 2 or 3, the transverse spatial coordinates are denoted by  $x_T = (x, y)$  for  $n=3$  or  $x_T = x$  for  $n=2$ ,  $\psi(x_T, z, \omega)$  is a single frequency component of a scalar wavefield at position  $(x_T, z)$ ,  $\varphi(k_T, z=0, \omega)$  is the Fourier transform (over  $x_T$ ) of the wavefield at position  $(x_T, z=0)$ ,  $(k_T, k_z)$  is the wavenumber vector,  $k_z z$  is the extrapolation phase shift, and the integral performs an inverse Fourier transform from  $k_T \rightarrow x_T$ . It is assumed that  $\psi(x_T, z, \omega)$  satisfies the constant-velocity Helmholtz equation and consists only of upward traveling waves. The vertical component of the wavenumber vector,  $k_z$ , in the phase shift can be calculated from the other components and the frequency by

$$k_z = \begin{cases} \sqrt{\frac{\omega^2}{v^2} - k_T^2}, & \frac{\omega^2}{v^2} > k_T^2 \text{ (wavelike)} \\ i\sqrt{k_T^2 - \frac{\omega^2}{v^2}}, & k_T^2 > \frac{\omega^2}{v^2} \text{ (evanescent)} \end{cases} \quad (2)$$

where  $v$  is the wave speed, and  $\varphi(k_T, z=0, \omega)$  is

$$\varphi(k_T, z=0, \omega) = \int_{-\infty}^{\infty} \psi(x_T, z=0, \omega) e^{ik_T x_T} dx_T. \quad (3)$$

In equation (1) the exponential term in square brackets accomplishes the wavefield extrapolation (by phase shift) and is known variously as *the wavefield extrapolation operator in the Fourier domain*, or *the symbol of the wavefield extrapolation operator*, or *the phase-shift operator*.

Equation (1) can be recast as an operation entirely in the space-frequency  $(x_T, \omega)$  domain as

$$\psi(x_T, z, \omega) = \int_{-\infty}^{\infty} \psi(\hat{x}_T, z=0, \omega) W_n(x_T - \hat{x}_T, z, v, \omega) d\hat{x}_T \quad (4)$$

where

$$W_n(x_T - \hat{x}_T, z, \omega) = \frac{1}{(2\pi)^{n-1}} \int_{-\infty}^{\infty} \hat{W}_n(k_T, z, \omega) e^{-ik_T(x_T - \hat{x}_T)} dk_T \quad (5)$$

with

$$\hat{W}_n(k_T, z, \omega) = e^{ik_z z} = \exp\left(iz\sqrt{\frac{\omega^2}{v^2} - k_x^2}\right) = \exp\left(iz\sqrt{k^2 - k_x^2}\right) \quad (6)$$

where the two rightmost forms show only the wavelike behavior of the square root. The evanescent behavior is still required and left implied.

$W_n$  is called *the wavefield extrapolator in the space frequency domain* or *the Schwartz kernel of the wavefield extrapolation operator*, and  $\hat{W}_n$  is its Fourier transform. The wavefield extrapolation operator includes  $W_n$  and the convolution integral of equation (4).

.As an aside, it is well-known that, for  $n = 3$ ,  $W_n$  has the exact form

$$W_3(r, z, k) = -\frac{ikz}{2\pi r^2} e^{ikr} \left(1 + \frac{i}{kr}\right) \quad (7)$$

where  $r = \sqrt{(x - \hat{x})^2 + (y - \hat{y})^2 + z^2}$  and  $k = \omega/v$ ; and for  $n = 2$

$$W_2(\rho, z, k) = -\frac{ikz}{\rho} H_1^{(1)}(k\rho) \quad (8)$$

where  $\rho = \sqrt{(x - \hat{x})^2 + z^2}$  and  $H_1^{(1)}$  is the first-order Hankel function of the first kind.

Thus far, the theory presented is exact but is applicable only for a homogeneous medium (e.g. constant velocity). To generalize to inhomogeneity, we assume, for a particular extrapolation step, say from 0 to  $z$ , that velocity is a function only of the transverse coordinates  $x_T$ . Variation of velocity with  $z$  will be accommodated by the usual process of taking smaller extrapolation steps. Thus we generalize equation (1) to

$$\psi(x_T, z, \omega) = \frac{1}{(2\pi)^{n-1}} \int_{-\infty}^{\infty} \varphi(k_T, z=0, \omega) \left[ e^{ik_z(x_T)z} \right] e^{-ik_T \cdot x_T} dk_T \quad (9)$$

where

$$k_z(x_T) = \begin{cases} \sqrt{\frac{\omega^2}{v(x_T)^2} - k_T^2}, & \frac{\omega^2}{v(x_T)^2} > k_T^2 \\ i \sqrt{k_T^2 - \frac{\omega^2}{v(x_T)^2}}, & k_T^2 > \frac{\omega^2}{v(x_T)^2} \end{cases} \quad (10)$$

The extrapolation formula in equation (9) is not exact and is characterized by Fishman and McCoy (1985) as a high-frequency approximation. Margrave and Ferguson (1999) identify it as the most accurate limit of the PSPI (phase-shift plus interpolation) process of Gazdag and Squazerro (1984) and therefore we call it *generalized* PSPI or GPSPI. Most known wave-equation depth migration schemes are approximations to GPSPI (note, however, that the *nonstationary phase shift* method or NSPS (Margrave and Ferguson, 1999) is the spatial transpose of GPSPI. Though equations (1) and (9) appear similar, the latter is much more expensive to implement numerically. This is because the integral in equation (1) is an inverse Fourier transform and can be accomplished with the FFT algorithm. The dependence of  $k_z$  on  $x_T$  in equation (9) means that it is not an inverse Fourier transform but is rather a *Fourier integral operator* (or *nonstationary filter*, Margrave, 1998) and can require much more computational effort.

GPSPI can be written in a form analogous to equation (4) as

$$\psi(x_T, z, \omega) = \int_{-\infty}^{\infty} \psi(\hat{x}_T, z=0, \omega) W_n(x_T, x_T - \hat{x}_T, z, \nu, \omega) d\hat{x}_T \quad (11)$$

where

$$W_n(x_T, x_T - \hat{x}_T, z, \omega) = \frac{1}{(2\pi)^{n-1}} \int_{-\infty}^{\infty} \left[ e^{ik_z(x_T)z} \right] e^{-ik_T \cdot (x_T - \hat{x}_T)} dk_T. \quad (12)$$

Equations (11) and (12) form the theoretical basis for the FOCI method. For fixed  $x_T$ , equation (12) is identical to the homogeneous result (equation (5)) and therefore our method invokes the *locally homogeneous* assumption.

### Operator stability

A fundamental characteristic of  $W_n$ , as given explicitly in equations (7) and (8), is that it is infinite in extent in the lateral coordinates  $x_T$ , that is the *support*<sup>1</sup> of  $W_n$  is non-compact. A fast and efficient wavefield extrapolation scheme can be developed from equations (11) and (12) if  $W_n$  can somehow be localized, that is if a compactly supported approximation,  $\tilde{W}_n$ , can be found. It is well established (e.g. Hale 1991) that localization such as

$$\tilde{W}_n(x_T, x_T - \hat{x}_T, z, \omega) = \Omega(x_T - \hat{x}_T) W_n(x_T, x_T - \hat{x}_T, z, \omega), \quad (13)$$

where  $\Omega(x_T - \hat{x}_T)$  is a symmetric, compactly supported, spatial window localized near  $x_T = \hat{x}_T$ , usually results in an unstable approximation. Here, instability means that, when equation (11) is applied repeatedly in a wavefield extrapolation process, the wavefield amplitude grows uncontrollably. To understand this effect, note that  $|\hat{W}_n| = 1, k^2 > k_x^2$  while  $\hat{W}_n = \exp(-z|k_z|) < 1, k^2 > k_x^2$ . The region  $k^2 > k_x^2$  is called *wavelike* while  $k^2 < k_x^2$  is called *evanescent*. Thus the Fourier-domain wavefield extrapolator changes behavior abruptly at the evanescent boundary ( $k^2 = k_x^2$ ). The windowing operation of equation (13) is a convolution of  $\hat{W}_n$  and  $\hat{\Omega}$  in the Fourier domain. Most compactly supported window choices cause  $|\hat{W}_n|$  to fluctuate slightly from the desired value of unity in the wavelike region. Suppose  $|\hat{W}_n| = 1 + \varepsilon, k^2 > k_x^2$  where  $|\varepsilon| \ll 1$ , then the application of this operator in  $m$  recursive steps results in  $|\hat{W}_n^m| = (1 + \varepsilon)^m \sim 1 + m\varepsilon$ . In the subsequent discussion, all operator designs will have nonzero  $\varepsilon$  and so are technically unstable. However, we will say an operator is *practically stable for  $m$  steps* if

<sup>1</sup> The support of a function is the closure of the domain over which the function is not identically zero. A function which vanishes outside a compact domain is said to have compact support.

$$\left| \hat{W}_n^m \right| \sim 1 + m\varepsilon < 1.2 \quad (14)$$

where 1.2 represents an arbitrary 20% tolerance. For example, if a depth migration is to be run with 10m steps to a depth of 5000m, then we require stability for  $m = 500$  steps. From equation (14) we infer that we must have  $|\varepsilon| < .2/500 = .0004$ . Thus we can tolerate an  $\hat{W}_n$  whose absolute value in the wavelike region departs from unity by not more than 4 parts in 10,000.

Meeting such a stability criterion as relation (14) has proven very difficult. The method of Hale (1991) does so by fitting a set of custom basis functions to an analytic Taylor series expansion of  $\hat{W}_n$ . The resulting operators are indeed stable, often for any number of steps. The difficulties with the Hale technique are that it is cumbersome to implement, difficult to change simple parameters like operator length, and the phase accuracy is often less than desired. Recently another method has been published by Thorbecke et al (2004). The Thorbecke method is much more flexible than Hale's and can be made sufficiently stable for many purposes. We review these two methods and compare them to FOCI in Al-Saleh et al (2004).

### A stabilizing Wiener filter

First we point out two useful properties of  $\hat{W}_n$ :

$$\hat{W}_n(k_T, z, \omega) = \hat{W}_n\left(k_T, \frac{z}{2}, \omega\right) \hat{W}_n\left(k_T, \frac{z}{2}, \omega\right) \quad (15)$$

and

$$\hat{W}_n^{-1}(k_T, z, \omega) = \hat{W}_n^*(k_T, z, \omega), \quad k^2 > k_x^2 \quad (16)$$

where the \* indicates the complex conjugate.

These properties can be utilized as follows. Let  $\tilde{W}_n(z/2)$  be a compactly supported approximation, in the sense of equation (13), (where we have suppressed all functional dependence except  $z$ ). Then we seek another compactly supported operator,  $WI_n$ , such that

$$WI_n \bullet \tilde{W}_n(z/2) = F^{-1} \left[ \left| \hat{W}_n(z/2) \right|^\eta \right] \quad (17)$$

where  $0 \leq \eta \leq 2$  is an adjustable parameter and  $F^{-1}$  symbolizes the inverse Fourier transform. The function of the right hand side of equation (17) is a zero-phase (we refer to phase in the  $k_T$  domain), band-limited approximation to a delta function. If  $\eta = 0$  it is truly a delta function and hence  $WI_n$  will be an inverse of  $\tilde{W}_n(z/2)$ . When  $\eta > 0$   $WI_n$  will be a *band-limited inverse* of  $\tilde{W}_n(z/2)$ . Since  $\tilde{W}_n(z/2)$  has half the phase of  $\tilde{W}_n(z)$ ,

and since  $WI_n$  has the negative of the phase of  $\tilde{W}_n(z/2)$  (regardless of the value of  $\eta$ ), we form the *FOCI approximation* to  $\tilde{W}_n(z)$  as

$$W_{nF}(z) = WI_n^* \bullet \tilde{W}_n(z/2) \approx W_n(z) \quad (18)$$

which follows from the approximate inverse nature of  $WI_n$  and from equations (15) and (16). As equation (18) shows, the FOCI operator is formed from the convolution of an approximate forward operator with the conjugate of its bandlimited inverse, hence the acronym FOCI. Since both  $\tilde{W}_n(z/2)$  and  $WI_n$  are compactly supported (by design) then so is  $W_{nF}$ .

Equation (17) is easily solved exactly in the Fourier domain, but the resulting  $WI_n$  will not have compact support. Therefore we solve equation (17) in the least-squares sense seeking a  $WI_n$  with specific compact support. Then  $W_{nF}$  will also have compact support that will be the sum of the supports of  $\tilde{W}_n(z/2)$  and  $WI_n$ .

Here we depart from the continuous notation used elsewhere in this paper and specify the discrete system equivalent to equation (17) appropriate for sampled data in 2D, and its least-squares solution as in Wiener filter theory. That is, equation (17) becomes

$$\begin{bmatrix} \tilde{W}_{2,0} & \tilde{W}_{2,1} & \cdots & \tilde{W}_{2,p} & 0 & \cdots \\ \tilde{W}_{2,1} & \tilde{W}_{2,0} & \tilde{W}_{2,1} & \cdots & 0 & \\ \vdots & \tilde{W}_{2,1} & \tilde{W}_{2,0} & \ddots & \tilde{W}_{2,p} & \\ \tilde{W}_{2,p} & \vdots & \tilde{W}_{2,1} & \ddots & \vdots & \\ 0 & \tilde{W}_{2,p} & \cdots & \ddots & \ddots & \tilde{W}_{2,1} \\ \vdots & & \ddots & & \tilde{W}_{2,0} & \\ 0 & & & & \vdots & \end{bmatrix} \begin{bmatrix} WI_{2,0} \\ WI_{2,1} \\ \\ \\ WI_{2,m} \end{bmatrix} = \begin{bmatrix} D_{2,0} \\ D_{2,1} \\ D_{2,2} \\ \vdots \\ D_{2,m+p} \end{bmatrix} \quad (19)$$

where  $\tilde{W}_{2,k}$ ,  $k \in [-p, -p+1, \dots, 0, \dots, p-1, p]$ , are the samples of a  $2p+1$ -length discrete version of  $\tilde{W}_2(z/2)$ ,  $WI_{2,k}$  are the samples of an  $2m+1$ -length unknown  $WI_2$ , and  $D_{2k}$  are the samples of the  $2m+2p+1$ -long Wiener *design function* which in this case is the discrete version of  $F^{-1} \left[ \left| \hat{W}_2(z/2) \right|^\eta \right]$ . Furthermore, in equation (19) we show only the center sample and positive lags of the full symmetric system. The matrix involving  $\tilde{W}_{2,k}$  in equation (19) is, of course, a symmetric Toeplitz convolution matrix. Written in abstract matrix notation, equation (19) is

$$\underline{\underline{\tilde{W}}}_2 \underline{WI}_2 = \underline{D}_2 \quad (20)$$

where the double underscore indicates a matrix and the single underscore a column vector. Matrix equation (20) is a linear system with  $m+1$  unknowns and  $m+p+1$

equations. It can be solved for any of the cases  $p < m, p = m, p > m$  by calculating the Moore-Penrose *pseudo-inverse* of  $\underline{\tilde{W}}_2$  called  $\underline{\tilde{W}}_2^{-g}$ .

$$\underline{W}I_2 = \underline{\tilde{W}}_2^{-g} \underline{D}_2 \quad (21)$$

Since matrix equation (20) always has more scalar equations than unknowns, we obtain a least-squares solution for  $\underline{W}I_2$ . Thus  $\underline{W}I_2$  is essentially a Wiener least-squares match filter that matches  $\underline{\tilde{W}}_2$  to the band-limited impulse  $\underline{D}_2$ . If  $\underline{D}_2$  were a perfect delta function, then  $\underline{W}I_2$  would be a true inverse to  $\underline{\tilde{W}}_2$ . Having obtained  $\underline{W}I_2$ , we calculate the full FOCI extrapolator with equation (18).

Some general features of this scheme are

1. The phase accuracy is limited by the initial estimate of the forward operator for a half-step,  $\tilde{W}_n(z/2)$ . The pseudo inverse designed by equation (21) or its 3D equivalent can, at best, negate this phase and so its conjugate can, at best, merely double the phase of  $\tilde{W}_n(z/2)$ . Therefore, the choice of  $p = \text{length}(\tilde{W}_n(z/2))$  should be made to obtain a desired phase accuracy.
2. Stability is generally enhanced by a longer  $WI_n$ . Though we have yet to fully explore this algorithm, we have determined that a good choice for  $m = \text{length}(WI_n)$  is  $m \geq 3p/2$ .
3. The parameter  $\eta$  (equation (17)) controls the degree of evanescent filtering in the final composite operator  $W_{nF}$  (equation (18)). Empirical testing reveals the not-surprising fact that larger values of  $\eta$  give operators that are less stable than those arising from smaller values. For  $\eta = 0$ , the resulting  $W_{nF}$  is all-pass (no evanescent filtering), while for  $\eta = 2$ ,  $W_{nF}$  has the full evanescent filtering expected from theory.
4. The length of  $W_{nF}$  in samples, is given by  $n_{op} = n_{for} + n_{inv} - 1$  where  $n_{for} = \text{length}(\tilde{W}_n)$  and  $n_{inv} = \text{length}(WI_n)$ .

### Dual operator tables for increased stability

The third feature mentioned in the list in the previous section gives rise to enhancement discussed here. Since evanescent filtering contributes to operator instability, it is natural to ask if it is required. Certainly, for a marching scheme in constant velocity, only the first few applications of the evanescent filter make any difference to the final result. This is because the wavenumber defining the evanescent boundary,  $k_{ev} = \pm\omega/v$ , does not change. It follows that repeated applications of the

evanescent filter in a constant velocity scenario only cause lessened stability. For the inhomogeneous case, we expect that it is similarly not necessary to apply the full evanescent filter on every step. Therefore, we construct two operator tables for use in any depth migration, a first table with strong evanescent filtering and a second with very little. This simply corresponds to the choice of two different  $\eta$  (equation (17)) values when constructing these tables. Then, for most extrapolation steps we use the second table corresponding to a small  $\eta$ , but for every  $j^{\text{th}}$  step, we use the first table with large  $\eta$ . Our empirical testing shows that, for small  $\eta$ , stability can be easily maintained for several thousand steps while for large  $\eta$ , it may only last for roughly 100 steps. A good choice is to invoke evanescent filtering every  $10^{\text{th}}$  step which easily leads to algorithms stable enough to reach 5000 or 10000 m depth.

### Spatial resampling

Most wavefield-extrapolation, depth-migration schemes use a fixed operator length that is independent of frequency. This is a potential problem for many datasets depending upon their frequency bandwidth and spatial sample size. In general, as frequency decreases, an operator of fixed size becomes increasingly problematic. Let  $\Delta x$  be the spatial sample size in the transverse coordinate in a 2D setting. Then the Nyquist wavenumber is  $k_{nyq} = \pi/\Delta x$  while the evanescent boundary is at  $k_{ev} = \omega/v$ . For a well-designed survey, we expect  $k_{ev} < k_{nyq}$  for all frequencies of interest but acknowledge that this is not always true. Now consider the spectral properties of an  $n_{op}$ -length approximate wavefield extrapolator, designed by any method. Since the spatial sample interval for the operator is also  $\Delta x$ , and assuming that  $n_{op}$  is an odd number, the Fourier transform of the operator will have samples at wavenumbers  $k_{xop} = \Delta k (0, \pm 1, \pm 2, \dots, \pm (n_{op} - 1)/2)$  where  $\Delta k = 2\pi/(n_{op}\Delta x)$ . That is, the operator has a sample at 0 wavenumber and then  $(n_{op} - 1)/2$  samples distributed out to just shy of  $+k_{nyq}$  in the positive wavenumber band and similarly for the negative wavenumbers. Thus, while the data may have hundreds of wavenumbers below  $k_{ev}$ , the operator may have only a few, or in the worst case only one (at zero), such wavenumbers. This becomes increasingly likely as frequency decreases or velocity increases. Thus a migration conducted with a fixed operator length, where typically  $n_{op}$  is a number like 21 or 31, will have many circumstances where most of the operator wavenumbers fall in the evanescent region. Such operators have poor phase control and are relatively unstable. This is clearly not an optimal circumstance.

There are two obvious solutions to this problem: (1) use an operator whose length is frequency dependent and increasing as frequency decreases, or (2) spatially resample the data at lower frequencies to a sample rate  $\Delta x' > \Delta x$ . We have investigated the former but have implemented the latter because it actually leads to increased stability and faster computation times. Procedurally, we require the specification of a frequency band of interest, say  $\omega_{mig} \in [\omega_{min}, \omega_{max}]$  and only deal with these frequencies. Then we break the  $[\omega_{min}, \omega_{max}]$  band into frequency “chunks”,  $n_{chunk}$  in number, given by

$$[\omega_{\min}, \omega_{\max}] = [\omega_{\min}, \omega_1) \cup [\omega_1, \omega_2) \cdots \cup [\omega_{nchunk-2}, \omega_{nchunk-1}) \cup [\omega_{nchunk-1}, \omega_{\max}] \quad (22)$$

and spatially resample the  $j^{\text{th}}$  chunk from  $\Delta x$  to  $\Delta x_j > \Delta x$  such that

$$\alpha \left( \frac{\pi}{\Delta x_j} \right) \leq \frac{\omega}{v_{crit}} \leq \beta \left( \frac{\pi}{\Delta x_j} \right), \quad \alpha < \beta \in [0,1], \quad \omega \in [\omega_{j-1}, \omega_j] \quad (23)$$

where  $v_{crit}$  is a velocity chosen to define the highest evanescent boundary of interest. A good, and always sufficient, choice for  $v_{crit}$  is  $v_{crit} = \min(v(x_T, z))$ , that is use the minimum velocity found anywhere in the velocity model. In our testing to date, we take  $\alpha = .7$  and  $\beta = .9$ . Thus we are always assured that at least 70% of the wavenumber samples of the operator fall within the wavelike region.

Since we are resampling to a coarser sample rate an anti-alias filter is required to avoid aliasing. The algorithm used for spatial resampling is important since we want to preserve data at the highest wavelike wavenumbers without any loss and utterly reject anything that is evanescent. Furthermore, we cannot tolerate ripples in the passband. The obvious choice is a truncation operation in the wavenumber domain where data at all wavenumbers greater than the new Nyquist are rejected and data at wavenumbers greater than  $\omega/v_{crit}$  are zeroed. If the data have  $n$  spatial locations before resampling and  $m_j < n$  wavenumbers are retained after resampling, it can be shown that the resulting spatial sample interval will be

$$\Delta x_j = \frac{n}{m_j} \Delta x \quad (24)$$

so the new sample interval is formed from the original by multiplication by a rational number.

### Implementation

We have constructed both post-stack and pre-stack 2D depth migration codes (in Matlab) based on the FOCI approach. In both cases, wavefield extrapolation is implemented as a nonstationary convolution according to (11) but using the FOCI approximate operator. That is we implemented

$$\psi(x, z, \omega) = \int_{-\infty}^{\infty} \psi(\hat{x}, z=0, \omega) W_{2F}(x, x-\hat{x}, z, v, \omega) d\hat{x}, \quad (25)$$

with the FOCI operator,  $W_{2F}$ , given by equation (18). Since the FOCI operator must be computed numerically, we followed the standard practice of building a table of such operators and implementing equation (25) through a table lookup procedure. Since, at any specific location, the operator only depends upon the ratio  $k = \omega/v$  the operator tables involve lookup in only one dimension. As discussed above, we actually build two

tables, corresponding to very little and significant evanescent filtering, and use the former for nine out of ten steps.

Since equation (25) is computed independently for each frequency, we implement spatial resampling (actually it is always down sampling) as needed to control the stability, and accuracy of the operators. We do not resample each frequency independently but rather break the data into frequency chunks such that the highest non-evanescent wavenumber for each chunk falls within the range of 70% to 90% of the Nyquist wavenumber. Since resampling depends upon the largest non-evanescent wavenumber, it actually is determined by the slowest velocity in the model. Since velocity typically increases with depth, it follows that the resampling could be repeated at a chosen set of depths to optimize efficiency and operator performance. Currently, we only resample once at the surface. Since the operator tables depend upon the spatial sample interval, we construct separate operator tables for each frequency chunk.

Our post-stack algorithm is a standard exploding reflector depth migration. Our pre-stack algorithm uses the shot-record migration paradigm.

## TESTING FOCI™

### Operator designs and time trials

Figure 1 shows a comparison of the truncated exact operator and the FOCI operator for the case of  $\Delta x = 10$ ,  $\Delta z = 10$ ,  $f = \omega / 2\pi = 30$ , and  $v = 3000$ . The truncated operator has 51 samples while the FOCI operators were both designed with  $n_{for} = 21$  and  $n_{inv} = 31$ . In the upper panel, two different FOCI designs are shown corresponding to  $\eta = 1$  and  $\eta = .01$ , the former giving have the evanescent filtering of the exact operator and the latter having very little evanescent filtering. In the middle panel, the *composite* FOCI operator refers to taking nine of every ten steps with the  $\eta = .01$  operator and one of every ten with the  $\eta = 1$  operator. Obviously, the FOCI operator has remained stable after 200 steps while the truncated operator has not. In the lower panel, the FOCI operator is seen to have significantly more phase error than the truncated operator. This is because, as mentioned previously, the phase accuracy of the FOCI operator is effectively determined by the length of the forward operator, which in this case was just 21 points.

The design situation shown in Figure 1 is actually a very non-optimal case as most of the operator points fall in the evanescent region. A much better case is seen in Figure 2 where all parameters are the same except that  $\Delta x = 35$ . (Note the scale change on the horizontal axis between the two figures.) Given a seismic dataset sampled at  $\Delta x = 10$ , the circumstance in Figure 2 can result with appropriate spatial down sampling. In Figure 2, approximately 80% of the operator wavenumbers fall below the evanescent boundary, and this leads to better stability and better phase accuracy.

Figures 3 and 4 show the operators in the space-frequency domain corresponding to Figures 1 and 2. The  $\Delta x = 35$  operators span a much greater spatial extent than the

$\Delta x = 10$  case and this allows the greater phase precision. Intuitively, if an operator is too short with respect to the data wavelengths, accuracy is lost.

We have also conducted time trials of the FOCI algorithm with and without spatial resampling and, for comparison, we also used the phase-shift algorithm. Of course, phase-shift is only a time migration method while FOCI is depth migration but the former is well known to show  $N \log N$  scaling (where  $N$  is the number of points in the dataset) so it is a good point of comparison. To conduct these tests, we generated a sequence of nine datasets with the number of traces starting at 32 and doubling each time until the ninth dataset which had 8192 traces. Thus we have scanned essentially three orders of magnitude of dataset size. Figure 5 plots the resulting run times on a 2.5 GHz PC (with lots of memory) versus the number of traces, while Figure 6 shows these same data on a log-log scale. From Figure 5, we can see that FOCI appears to be faster than phase shift, and that spatial down-sampling appears to speed FOCI up by about 20%. The conclusion that FOCI is faster than phase shift may be unjustified and could simply be due to the fact that our FOCI algorithm has received more attention than our phase-shift code. However, the 20% speedup due to spatial resampling is probably real.

We show separately the time required for building the operator tables in FOCI. For small datasets, this time is a significant fraction of the total time but it rapidly becomes negligible as the dataset size increases.

Since direct comparisons of run times can be strongly dependent upon the quality of the code being compared, it is often preferable to assess how the run times scale with increasing dataset size. The log-log plot of Figure 6 facilitates this. If the run times scale as  $N^\sigma$  then the slope of the line on Figure 6 should be  $\sigma$ . It is apparent that all three algorithms scale slightly slower than order  $N^1$  and are well faster than order  $N^2$ . Over the range of values in this experiment, scaling like  $N \log N$  corresponds to a  $\sigma$  of about 1.25 (assuming natural logarithms). Figure 6 suggests that all three algorithms scale similarly for large  $N$  with  $\sigma$  near 1.1.

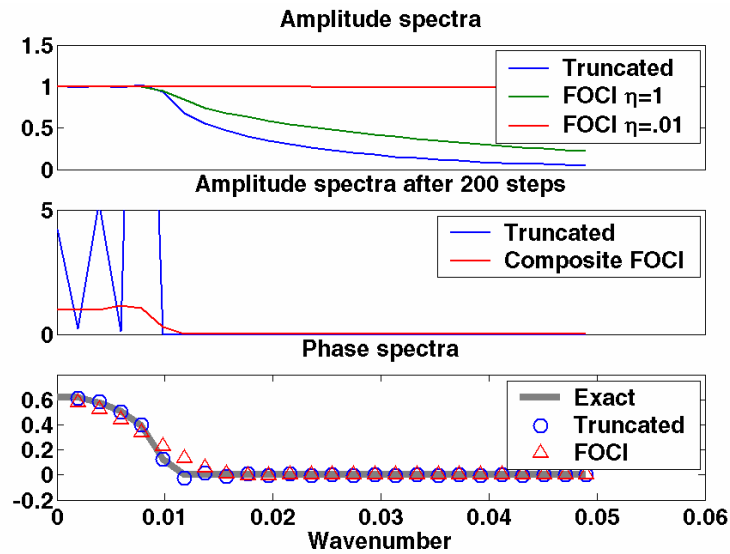


FIG. 1. The amplitude spectra of three different 51 point approximations to the exact wavefield extrapolator are shown (top). All curves are for  $\Delta x = 10$  and other relevant parameters are discussed in the text. These spectra are then raised to the power 200 (center) to simulate taking 200 steps. The curve labeled “composite FOCI” refers to taking 20 steps with the  $\eta = 1$ .

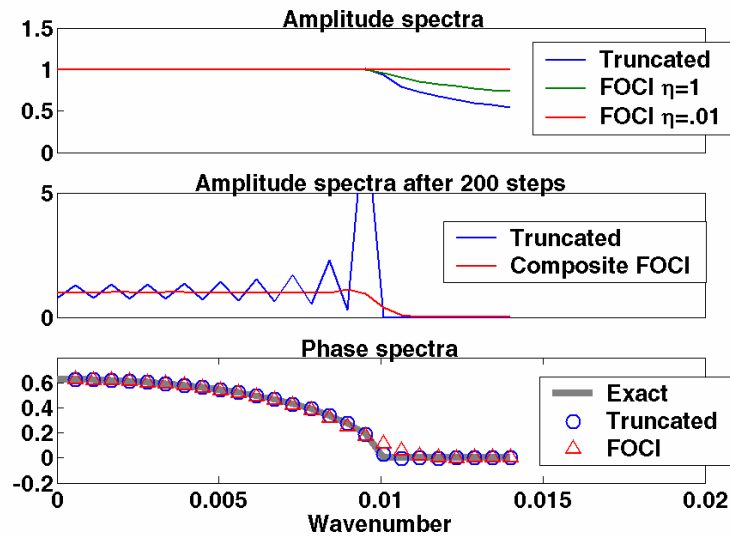


FIG. 2. Similar to Figure 1 except that  $\Delta x = 35$ . Note the horizontal scale change.

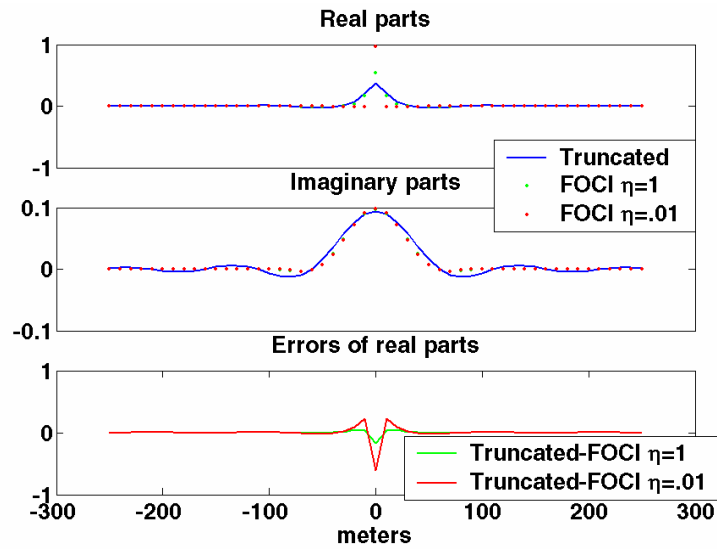


FIG. 3. The space-frequency domain view of the operators depicted in Figure 1. In the upper panel we show the real parts while the imaginary parts are in the lower. The bottom panel shows differences for the real parts only. This should be compared with Figure 4 while noting the horizontal scale change.

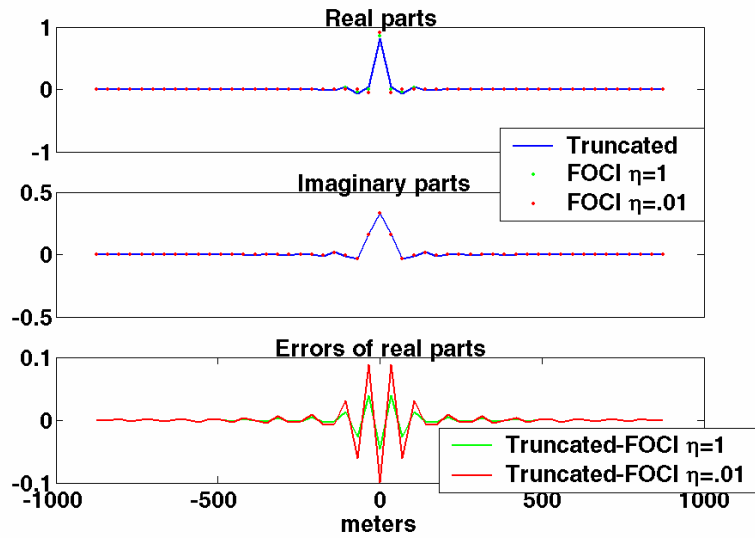


FIG. 4. The space-frequency domain view of the operators depicted in Figure 2. In the upper panel we show the real parts while the imaginary parts are in the lower. The bottom panel shows differences for the real parts only. This should be compared with Figure 3 while noting the horizontal scale change.

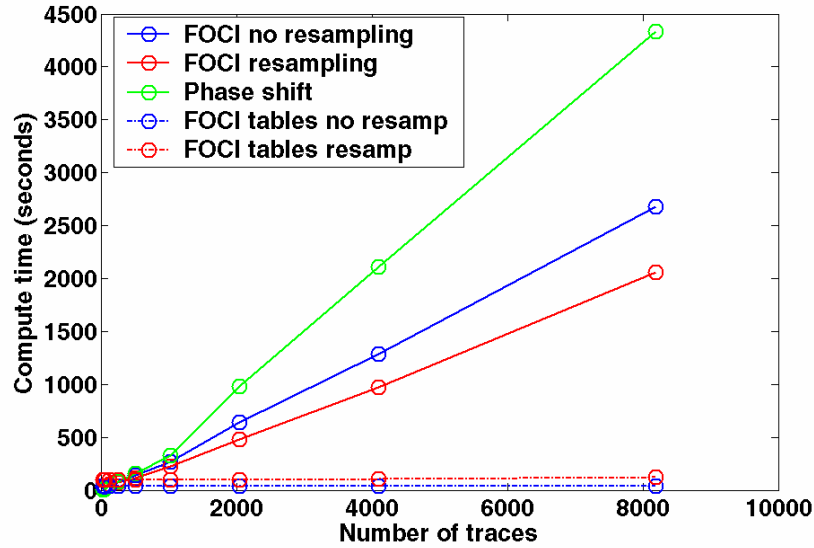


FIG. 5. The compute time (in seconds) for a series of test datasets spanning three orders of magnitude in size.

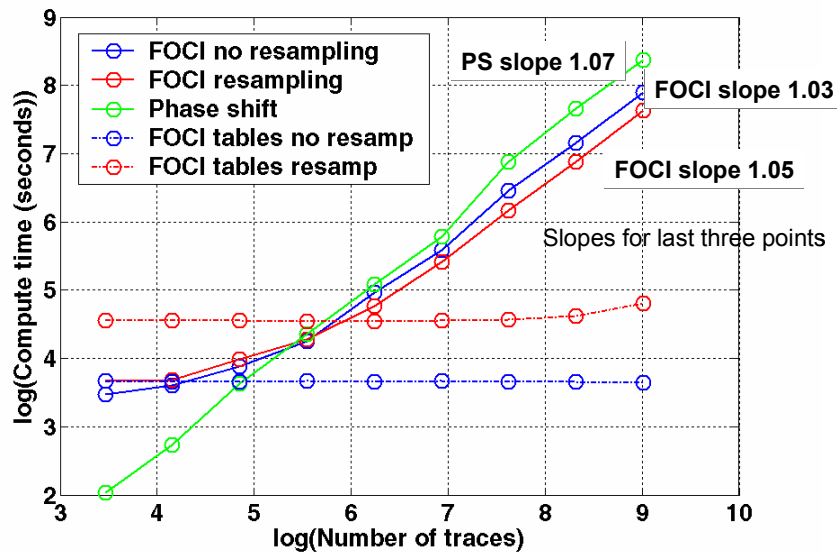


FIG. 6. Similar to Figure 5 except the data are displayed on a log-log scale. The estimated slopes are the estimate of the power of  $N$  that controls the algorithm scaling. So all three algorithms appear to be scaling roughly as  $O(N^1)$ .

### Impulse responses and post-stack synthetics

Figure 7 shows the impulse response of the phase-shift algorithm for a particular velocity and geometry. The input was a set of six impulses on the center trace. In Figure 7 we show the result from the FOCI algorithm where no spatial resampling has been done. The FOCI operator was the composite of a 7 point forward operator ( $n_{for} = 7$ ) and a 15 point inverse operator ( $n_{inv} = 15$ ). This should be contrasted with the result in Figure 9 where exactly the same FOCI parameters were used but spatial resampling was

also employed. It is apparent that the “exact” phase shift result is much better approximated when spatial resampling is employed.

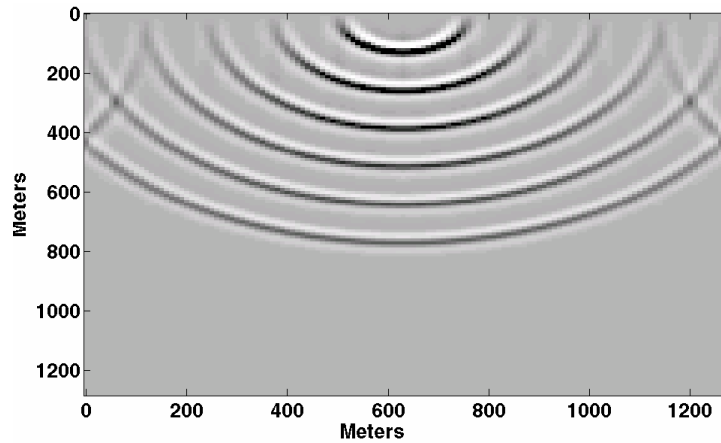


FIG. 7. The response of the phase shift algorithm to a set of six band-limited impulses placed in the center trace.

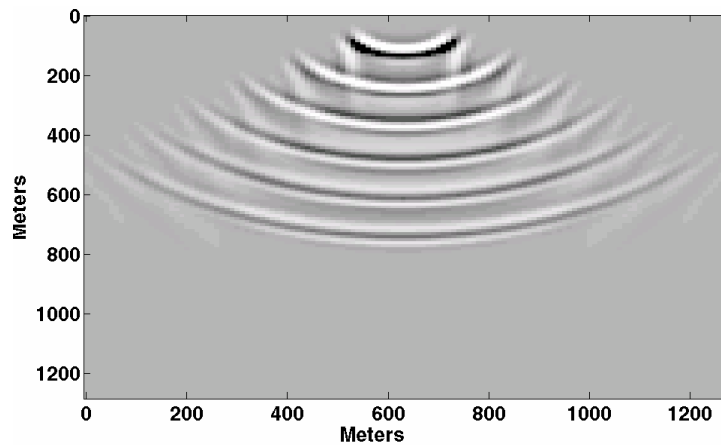


FIG. 8. The response of a 21 point FOCI operator ( $n_{for} = 7$ ,  $n_{inv} = 15$ ) to the same input as Figure 7. This version of FOCI did not employ spatial resampling.

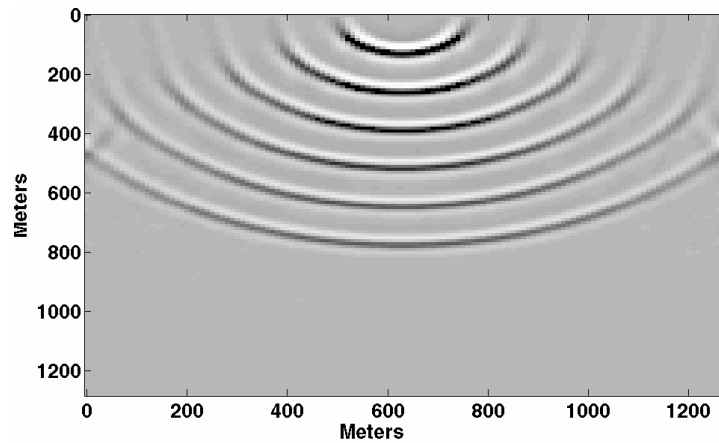


FIG. 9. Similar to Figure 8 except that the FOCI algorithm included spatial resampling. Compare with Figures 7 and 8.

To test the post-stack depth migration an exploding reflector synthetic was created from the Marmousi velocity model. The velocity model is shown in Figure 10 while the exploding reflector synthetic seismic section is shown in Figure 11. The Marmousi velocity model is sampled on a 10 m grid and the exploding reflector seismogram was created with the CREWES finite-difference toolkit (in Matlab) using a second-order time-stepping scheme. The data are sampled at .004 seconds and a 5/10-40/50 Ormsby wave has been applied.

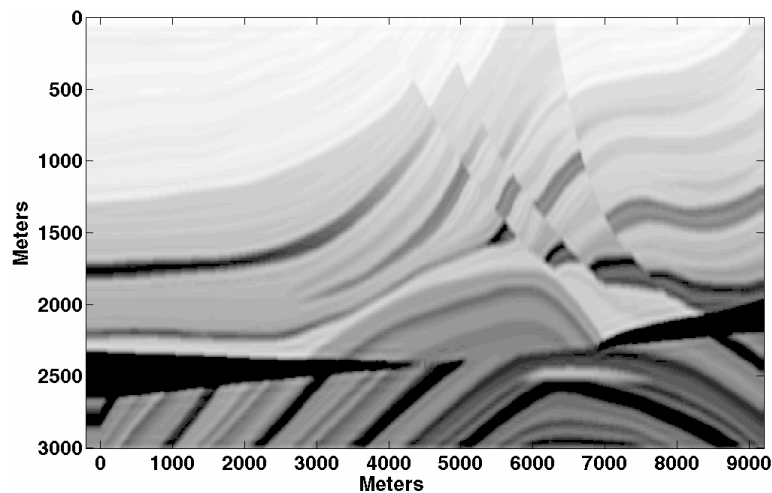


FIG. 10. The velocity model for the Marmousi structure is shown. Dark is a high velocity and light gray is a low velocity. The exploration target is a low velocity lens at about  $(x,z)=(6500,2700)$ .

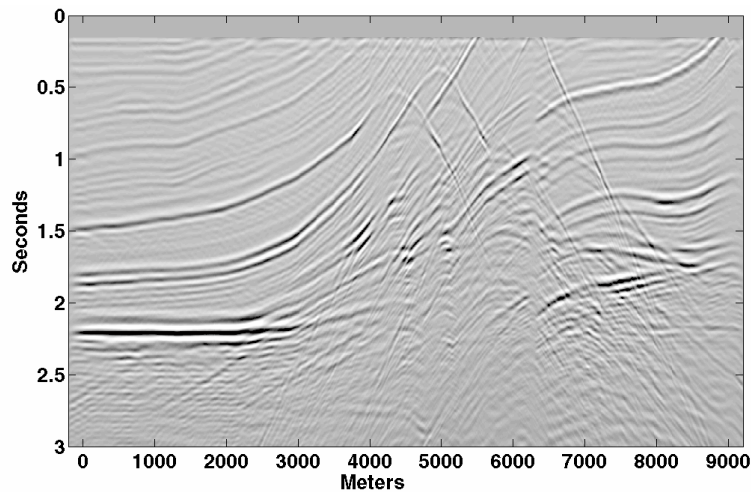


FIG. 11. An exploding reflector seismogram resulting from the velocity model of Figure 10. This was created by a second-order finite-difference method and has a 5/10-40/50 Ormsby wavelet applied.

Two different results from the FOCI method are shown in Figures 12 and 13. In Figure 12, a 51 point operator described by the parameters  $n_{for} = 21$ ,  $n_{inv} = 31$ , and  $n_{win} = 51$ . The last parameter refers to the length of a Hanning window that was applied to the final design. In Figure 13, the parameters are the same except that  $n_{win} = 21$ . The longer operator gives a slightly better image, especially near the exploration target

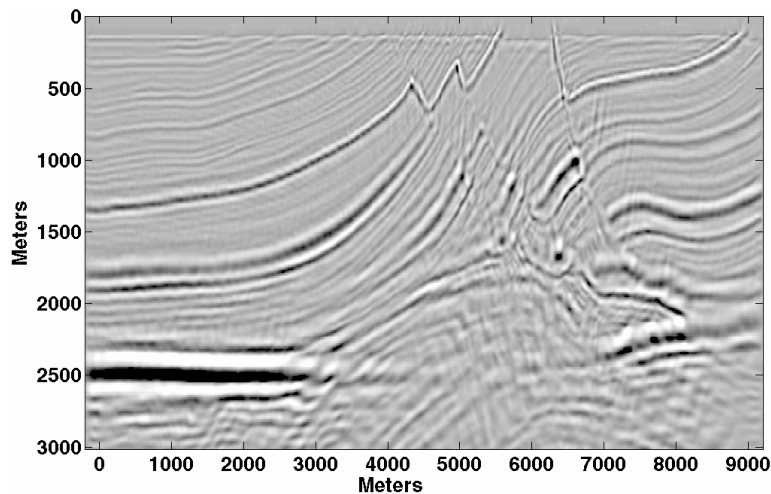


FIG. 12. A FOCI migration of the seismogram of Figure 11 using the velocity model of Figure 10. The migration was done with a 51 point operator described by the parameters  $n_{for} = 21$ ,  $n_{inv} = 31$ , and  $n_{win} = 51$ .

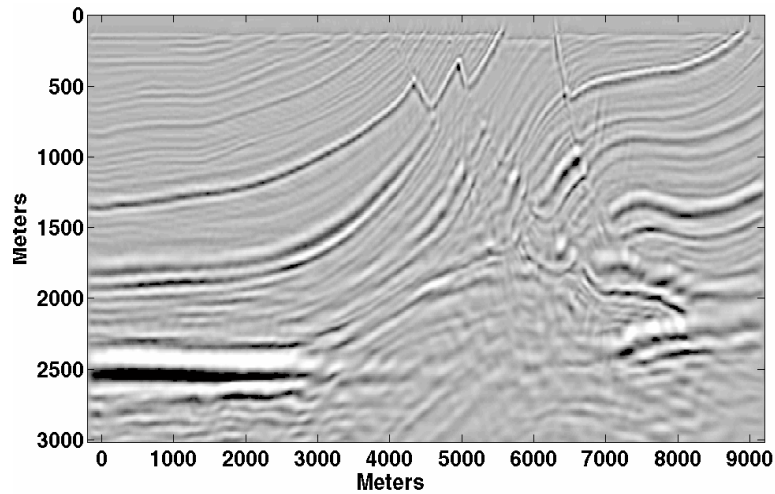


FIG. 13. Similar to Figure 12 except that a 21 point operator was used described by the parameters  $n_{for} = 21$ ,  $n_{inv} = 31$ , and  $n_{win} = 21$ .

### Pre-stack Marmousi migrations

We have conducted a series of tests of the FOCI algorithm in imaging the Marmousi structure with prestack depth migration. In Al-Saleh et al (2004), we compare the FOCI algorithm with Hale's and Thorbecke's methods. Here we simply show a few results to demonstrate that good images are obtained.

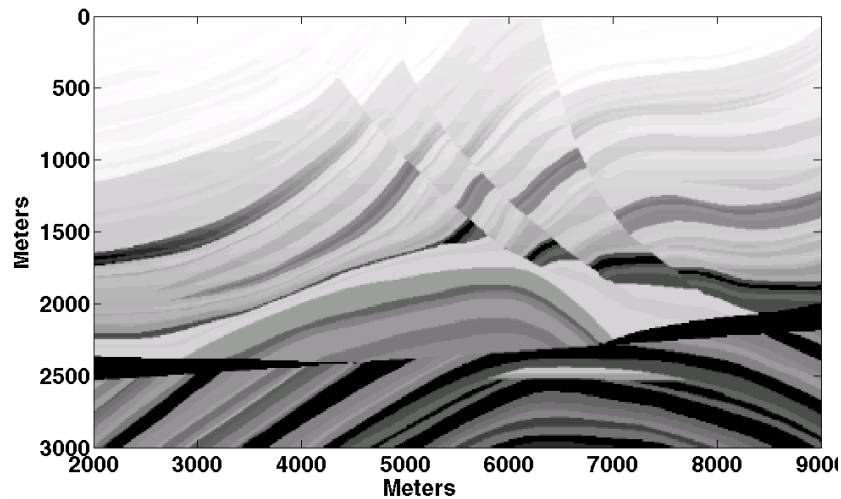


FIG. 14. The Marmousi velocity model sampled at 12.5 meters.

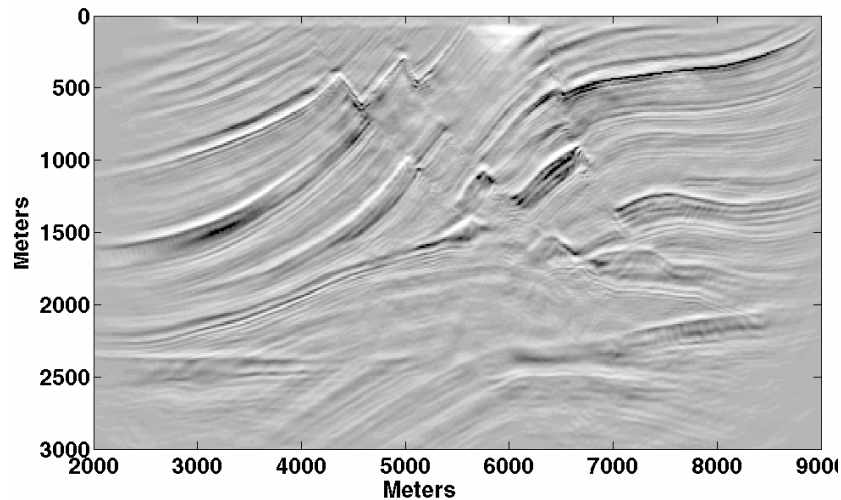


FIG. 15. A prestack depth migration of the Marmousi dataset using the velocity model of Figure 14. The data were migrated into a 12.5 m grid.

In Figure 14 we show again the Marmousi velocity model as appropriate for comparison with our pre-stack depth migration results. In Figure 15 we show one of our best results to date with the FOCI algorithm. There is a very good agreement between the structural detail in the image and in the velocity model. This image is a stack of all 240 migrated shot records in the Marmousi dataset. Each shot record was migrated independently with the FOCI algorithm using a 51 point operator described by the parameters  $n_{for} = 21$ ,  $n_{inv} = 31$ , and  $n_{win} = 0$ . In the latter case, the setting  $n_{win} = 0$  means that the final FOCI operator was used without any post-design windowing. This creates a more accurate operator but possibly at the expense of lessened stability. The migration required about 20 hours on a single 2.5 GHz PC.

There is a significant algorithmic artifact present in Figure 15 whose amelioration is the subject of current research. At the top of the image near x coordinate 6000 is a white blob. Testing has shown that this results from evanescent energy that has not been fully suppressed. There are other, more subtle, examples of image blurring from this effect elsewhere in the image.

Figure 16 shows a zoom of the central part of Figure 15 to show the kind of detail found in the image. This can be compared with Figure 17, which shows an approximation of the Marmousi reflectivity. This reflectivity was calculated with the expression  $r(x, z) = \text{sgn}\left(\frac{\partial}{\partial z} \ln v(x, z)\right) \left| \vec{\nabla} \ln v(x, z) \right|$ . It is apparent that most of the detail in the reflectivity has been resolved.

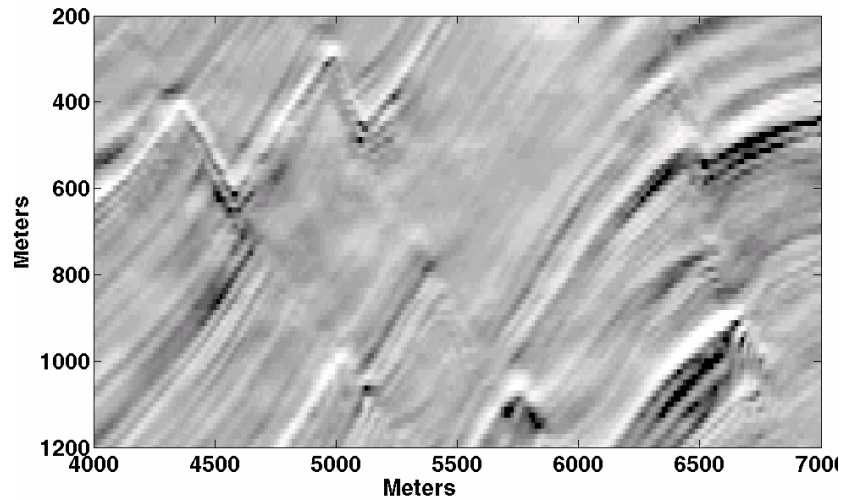


FIG. 16. This shows a detail of the central faulted area from Figure 15.

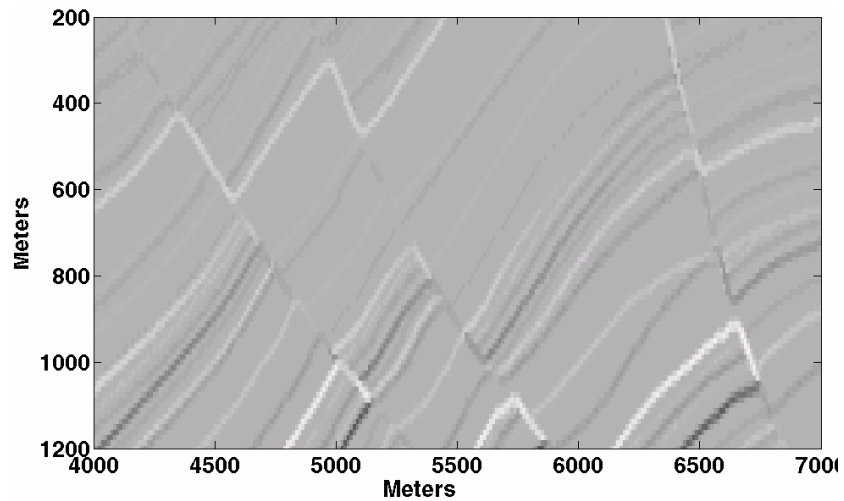


FIG. 17. This is the approximate Marmousi reflectivity for the same area that is imaged in Figure 16.

## CONCLUSIONS

We have presented a new algorithm for constructing a compactly supported, explicit, space-frequency domain depth migration operator. The operator is designed by first truncating the exact operator for a half-depth-step to a desired length and then designing a fixed-length, least-squares, band-limited inverse for the truncated operator. The final FOCI operator is formed from the convolution of the forward operator with the conjugate of its inverse. We have demonstrated that this operator can be constructed with good stability and phase accuracy. We have then implemented pre and post stack explicit depth migrations with this operator design. Significant innovations in our depth migration algorithms are the use of dual operator tables, with low and high levels of evanescent filtering, and spatial down-sampling of the lower frequencies. These innovations increase operator accuracy and stability as well as shorten the overall computation time. Testing of this algorithm shows that it scales approximately as order

$N$  over at least three orders of magnitude of dataset size. Excellent images are now being obtained with both pre and post stack depth migration.

### ACKNOWLEDGEMENTS

We thank the industrial sponsors of both the *CREWES* and *POTSI* projects. We also thank *NSERC*, *MITACS*, and *PIMS* for their funding assistance.

### NOTICE OF PATENT APPLICATION

A US patent for the FOCI™ process has been applied for. The patent mentions the design of a stable operator by the forward-operator-conjugate-inverse method, the use of dual operator tables to reduce evanescent filtering, and spatial down-sampling as a method to increase operator performance and reduce computation time.

### REFERENCES:

- Al-Saleh, S. M., Margrave, G. F., and Geiger, H. D., 2004, The FOCI method versus other extrapolation methods: This volume.
- Fishman, L., and McCoy, J. J., 1985, A new class of propagation models based on a factorization of the Helmholtz equation: *Geophys. J. astr. Soc.*, **80**, 439-461.
- Gazdag, J., 1978, Wave equation migration with the phase-shift method: *Geophysics, Soc. of Expl. Geophys.*, **43**, 1342-1351.
- Gazdag, J., and Squazzerro, P., 1984, Migration of seismic data by phase shift plus interpolation: *Geophysics*, **49**, 124-131.
- Hale, D., 1991, Stable explicit extrapolation of seismic wavefields: *Geophysics*, **56**, 1770–1777.
- Margrave, G. F., 1998, Theory of nonstationary linear filtering in the Fourier domain with application to time variant filtering: *Geophysics*, **63**, 244-259.
- Margrave, G. F. and Ferguson, R. J., 1999, Wavefield extrapolation by nonstationary phase shift: *Geophysics*, **64**, 1067-1078.
- Thorbecke, J. W., Wapenaar, K., and Swinnen, G., 2004, Design of one-way wavefield extrapolation operators, using smooth functions in WLSQ optimization.